Arch Appl Mech (2010) 80: 569–580
DOI 10.1007/s00419-009-0384-0

SPECIAL ISSUE

Serdar Göktepe · Jonathan Wong · Ellen Kuhl

Atrial and ventricular fibrillation: computational simulation of spiral waves in cardiac tissue

Received: 13 November 2008 / Accepted: 25 September 2009 / Published online: 25 October 2009

Abstract This manuscript proposes a novel, efficient finite element solution technique for the computational simulation of cardiac electrophysiology. We apply a two-parameter model that is characterized through a fast action potential and a slow recovery variable. The former is introduced globally as a nodal degree of freedom, whereas the latter is treated locally as internal variable on the integration point level. This particular discretization is extremely efficient and highly modular since different cardiac cell models can be incorporated straightforwardly through only minor local modifications on the integration point level. In this manuscript, we illustrate the algorithm in terms of the Aliev–Panfilov model for cardiomyocytes. To ensure unconditional stability, a backward Euler scheme is applied to discretize the evolution equation for both the action potential and the recovery variable in time. To increase robustness and guarantee optimal quadratic convergence, we suggest an incremental iterative Newton–Raphson scheme and illustrate the consistent linearization of the weak form of the excitation problem. The proposed algorithm is illustrated by means of two- and three-dimensional examples of re-entrant spiral and scroll waves characteristic of cardiac arrhythmias in atrial and ventricular fibrillation.

Keywords Electrophysiology · Excitation · Finite elements · Re-entry · Spiral waves · Scroll waves · Aliev–Panfilov model

1 Motivation

Atrial and ventricular fibrillation are common forms of cardiac arrhythmias characterized through an abnormal electric activity of the heart. In the United States alone, almost half a million people die each year as a result of cardiac arrhythmias; arrhythmias are a leading risk factor for stroke which, in turn, is the leading cause of long-term disability and the third leading cause of death [1,35]. Treatment of cardiac arrhythmias can either be pharmacological, e.g., based on the antiarrhythmetic drugs, or interventional, e.g., in the form of implantable defibrillators, bi-ventricular pacing, or catheter ablation. Despite tremendous scientific improvements during the past 20 years, the treatment of cardiac arrhythmias is far from being fully understood and the choice of the

S. Göktepe · J. Wong · E. Kuhl
Department of Mechanical Engineering,
Stanford University, 496 Lomita Mall, Stanford, CA 94305, USA
E-mail: goktepe@stanford.edu

J. Wong
E-mail: jonjwong@stanford.edu

E. Kuhl (✉)
Departments of Bioengineering, and Cardiothoracic Surgery,
Stanford University, 496 Lomita Mall, Stanford, CA 94305, USA
E-mail: ekuhl@stanford.edu

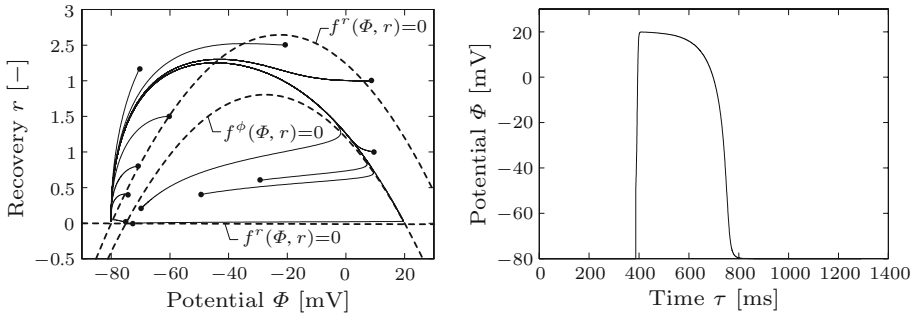

Fig. 1 Two-parameter Aliev–Panfilov model for cardiac excitation with $\alpha = 0.05$, $\gamma = 0.002$, $b = 0.15$, $c = 8$, $\mu_1 = 0.2$, and $\mu_2 = 0.3$. Original non-dimensional action potential ϕ and time t are scaled to physiological action potential Φ and time τ as $\Phi = [100\phi - 80]\,\text{mV}$ and $\tau = [12.9t]\,\text{ms}$. Phase portrait with *dashed lines* illustrating nullclines with $f^\phi = 0$ and $f^r = 0$ (*left*). Non-oscillatory action potential of cardiomyocytes characterized through a fast upstroke and a long plateau upon excitation by external stimulation $f^\phi_{\text{stim}} = 30\,\text{mV}$ from the steady state $\Phi_0 = -80\,\text{mV}$, $r_0 = 0$ (*right*)

appropriate treatment strategy still strongly relies on the personal experience of the individual cardiologist. The goal of this manuscript is to develop a computational framework that enables the simulation of the electrical excitation of the heart to provide a better understanding of cardiac arrhythmias and ultimately guide the patient-specific selection of the most effective treatment strategy.

In the normal heart, rhythmic cardiac contraction is coordinated through non-linear electrical waves of excitation that smoothly propagate through the cardiac tissue. Even slight disturbances of the complex electrical conduction system can have devastating physiological consequences and initiate conditions under which the tissue re-excites itself through re-entrant spiral waves, see, e.g., the early experimental investigations of Mines [19], or the modern analytical and computational studies by Fenton et al. [7,8], Nash and Panfilov [21], Panfilov et al. [24,25], Rogers and McCulloch [27–29], and Sermesant et al. [32,33]. The uncoordinated propagation of excitation waves within closed circuits typically manifest itself in a fast, uncoordinated, arrhyhthmic contraction of the heart and a severe loss of pump function, see, e.g., the illustrative textbooks of Ganong [10], Klabunde [16], or Plonsey and Barr [26].

Although the origin of fibrillation seems to be well understood, there is still no general agreement on a unified reliable medical treatment for cardiac arrhythmias. The complex interplay of cellular inhomogeneities, altered refractoriness, action potential duration, and restitution kinetics is thus essential to understand the electrophysiological origins of fibrillation and to optimize the design therapies that successfully control atrial and ventricular rhythm disorders. The electrical activity of cardiac cells is governed by a balance between the electrical and chemical gradients across the outer membrane of a the cell. These gradients are caused by the selective permeability of the cell membrane to different ions at different points in throughout the cardiac cycle. At rest, the transmembrane potential is approximately $-80\,\text{mV}$ (see Fig. 1). The cell can be excited by an electrical stimulus that generates an initial depolarization across the cell membrane. Once the stimulus exceeds a threshold of about $-50\,\text{mV}$, the transmembrane potential increases rapidly from the resting state of $-80\,\text{mV}$ to the excited state of approximately $+20\,\text{mV}$, see, e.g., Berne and Levy [4], Bers [5], Opie [23], and Hunter et al. [14]. This change in transmembrane potential is brought about by the interaction of different ion channels controlling the inward and outward flux of charged sodium, potassium, and calcium ions. The first model to quantitatively describe the electrophysiology of excitable cells was proposed by Hodgkin and Huxley [13] more than half a century ago. Most currently available cardiac cell models were derived from the classical Hodgkin–Huxley model that had originally been developed for nerve cells. The Hodgkin–Huxley model was significantly simplified by FitzHugh [9] and Nagumo et al. [20] in the early 60s. Next to the fast action potential ϕ, the two-parameter FitzHugh–Nagumo model is characterized through a slow recovery variable r that phenomenologically captures the effects of all ionic currents in one single variable (see Fig. 1). Numerous refinements of the FitzHugh–Nagumo model have been presented in the past to account for the specific depolarization repolarization characteristics of different cell types, see, e.g., Noble [22], Beeler and Reuter [3], and Luo and Rudy [18], for the original models, and Clayton and Panfilov [6], Keener and Sneyd [15], Sachse [30], and ten Tuscher and Panfilov [34] for excellent comparisons of the different approaches.

For the simulation of arrythmias on the tissue or organ level that we have in mind as primary application of our algorithm, it is not necessary to represent all ionic currents of the cell with the accuracy and complexity of the biophysically exact models cited above. Rather, we seek to reproduce the fundamental characteristics of the action potential at minimal computational cost. To this end, we apply the phenomenological two-parameter

Aliev–Panfilov model [2] which is based on slight modifications of the original FitzHugh–Nagumo model. It is particularly tailored to model the fast upstroke and the extended action potential plateau of ventricular cardiomyocytes. Thus far, the Aliev–Panfilov has primarily been combined with finite difference solution schemes. We present a recently developed finite element algorithm for the excitation of cardiac tissue (see [11]), that can be generalized straightforwardly to a fully coupled excitation–contraction formulation (see [12]) suited for whole heart models as sketched by Kotikanyadanam et al. [17]. In this manuscript, particular focus is placed on illustrating the performance of this novel approach in the context of two-dimensional spiral wave and three-dimensional scroll wave formations in classical benchmark domains, and in a generic bi-ventricular heart model.

The manuscript is organized as follows: Sect. 2 briefly summarizes the governing equations of the fast excitation problem and the slow recovery problem. Section 3 then illustrates the computational solution algorithm based on a global node point based solution of the excitation problem combined with a local integration point based solution of the recovery problem. Section 4 documents the features of the proposed algorithm in the context of two-dimensional spiral waves and three-dimensional scroll waves of excitation. The manuscript closes with final discussions and comments in Sect. 5.

2 Governing equations

Excitable biological tissues can be characterized through a coupled system of equations for the fast action potential ϕ and the slow recovery variable r whereby the latter phenomenologically summarizes the effects of charged sodium, potassium, and calcium currents. In this section, we briefly reiterate the set of governing equations of cardiac electrophysiology based on the Aliev–Panfilov model [2].

2.1 The excitation problem

The excitation problem characterizes the spatio-temporal evolution of the action potential ϕ. In its generalized form, it can be expressed as follows:

$$\dot{\phi} = \operatorname{div} \boldsymbol{q}(\phi) + f^{\phi}(\phi, r) \tag{1}$$

Herein, the original local FitzHugh–Nagumo equations have been enhanced by the flux term $\operatorname{div} \boldsymbol{q}(\phi)$ in terms of the flux vector $\boldsymbol{q}$ with

$$\boldsymbol{q} = \boldsymbol{D} \cdot \nabla \phi \tag{2}$$

to account for the propagation of the action potential to adjacent cells via gap junctions located on the intercalated disk. Diffusion is characterized phenomenologically through the second-order diffusion tensor $\boldsymbol{D} = d^{\text{iso}}\boldsymbol{I} + d^{\text{ani}}\boldsymbol{n} \otimes \boldsymbol{n}$ whereby d^{iso} and d^{ani} determine the degree of isotropic and anisotropic diffusion, respectively. The source term f^{ϕ}

$$f^{\phi} = c\,\phi\,[\phi - \alpha][1 - \phi] - r\,\phi \tag{3}$$

collectively summarizes the characteristic cubic contribution $c\,\phi\,[\phi - \alpha][1 - \phi]$ in terms of the action potential itself, and the coupling to the phenomenological recovery variable r. The parameter α represents an oscillation threshold. Cardiomyocytes display a stable action potential represented through positive α values, $\alpha > 0$. Upon perturbation away from the stable state, the fast and slow variables travel through a four-phase cycle of the regenerative, the active, the absolutely refractory, and the relatively refractory phases (see Fig. 1). After this cycle, the membrane potential returns to its stable state below the critical excitation threshold. In the healthy tissue, a new excitation cycle is initiated by an external stimulus through a traveling excitation wave. In Sect. 4, we will demonstrate that fibrillation can be caused by spiral and scroll waves of excitation where otherwise stable tissue is continuously re-excited when the refractory period is significantly shortened; this suppresses the necessary relaxation of the heart during the filling phase.

2.2 The recovery problem

The slow-recovery variable r is governed through a local evolution equation

$$\dot{r} = f^{r}(\phi, r) \tag{4}$$

which is coupled to the action potential ϕ through the source term f^r.

$$f^r = \left[\gamma + \frac{\mu_1\, r}{\mu_2 + \phi}\right] [-r - c\,\phi\,[\phi - b - 1]] \tag{5}$$

In contrast to the original FitzHugh–Nagumo model, the additional weighting factor $[\,\gamma + \mu_1\, r\,/\,\mu_2 + \phi\,]$ has been introduced by Aliev and Panfilov [2] to phenomenologically tune the restitution curve to experimental observations by adjusting the parameters μ_1 and μ_2. Since diffusion of the action potential is typically assumed to be dominant over diffusion of the recovery variable, the evolution equation (4) for the recovery variable is assumed to be strictly local.

Remark 1 (FitzHugh–Nagumo equations) The system of Eqs. (1) and (4) represents the classical FitzHugh–Nagumo equations [9,20] for the particular choice of $f^\phi = c\,[\,\phi\,[\,\phi - \alpha\,]\,[\,1 - \phi\,] - r\,]$ and $f^r = \phi - b\,r + a$. In contrast to the more complex Aliev–Panfilov model, coupling of the action potential and the recovery variable is simply linear for the FitzHugh–Nagumo model. For a negative oscillation threshold $\alpha < 0$, the FitzHugh–Nagumo equations can be applied to simulate rhythmically discharging self-oscillatory pacemaker cells such as the sinoatrial or the atrioventricular node, see Göktepe and Kuhl [11] for a realization of the FitzHugh–Nagumo model within the same algorithmic framework proposed herein.

Remark 2 (Dimensional scaling for cardiomyocytes) In the above formulation, Eqs. (1) and (4) are obviously non-dimensional. Aliev and Panfilov [2] have suggested to scale the non-dimensional action potential ϕ and time t through $\Phi = [\,100\phi - 80\,]\,\text{mV}$ and $\tau = [\,12.9t\,]\,\text{ms}$ to obtain the physiological action potential amplitude Φ (mV) ranging from -80 to $+20\,\text{mV}$ and the characteristic excitation time τ (ms) for cardiomyocytes of about 300 ms, compare Fig. 1.

Remark 3 (Notion of excitation waves) From a mathematical point of view, the combination of Eqs. (1) and (2) yields a second-order partial differential equation $\dot{\phi} = \text{div}\,(\boldsymbol{D}\cdot\nabla\phi) + f^\phi(\phi, r)$ which is of parabolic nature. Strictly speaking, the term 'wave' which is typically associated with the propagating signal of electric excitation is incorrect, since waves are characteristic of hyperbolic equations. Nevertheless, the notion 'excitation wave' has been established in the medical community and is mis-used similar to, e.g., the term 'heat wave' in the meterology community although the underlying terms do not reflect waves in an mathematical sense.

3 Computational algorithm

We propose to discretize the spatio-temporal excitation problem with the help of a finite difference based classical backward Euler scheme in time combined with a finite element solution in space. For the latter, the action potential ϕ is introduced as global degree of freedom at the node point level, whereas the recovery variable r is introduced locally as internal variable on the integration point level. The underlying computational algorithm is presented in the sequel.

3.1 The excitation problem: global solution at the node point level

The strong residual form $\mathsf{R}^\phi = \dot{\phi} - \text{div}\,(\boldsymbol{q}) - f^\phi \doteq 0$ of the non-linear excitation equation (1) constitutes the basis for the finite element formulation of electrophysiology in the domain of interest $\mathcal{B}$. It is complemented by the Dirichlet boundary conditions $\phi = \bar{\phi}$ on $\partial\mathcal{B}_\phi$ and the Neumann boundary conditions for the flux $\boldsymbol{q}\cdot\boldsymbol{n} = \bar{q}$ on $\partial\mathcal{B}_q$. For most physiologically relevant excitation problems, homogeneous Neumann boundary conditions $\boldsymbol{q}\cdot\boldsymbol{n} = 0$ have been applied on the entire boundary $\partial\mathcal{B}$. The weak form of the above residual statement and the corresponding Neumann boundary conditions is obtained through an integration over the domain $\mathcal{B}$, multiplication with the scalar-valued test function $\delta\phi$, integration by parts, and application of Gauss' theorem. For the spatial discretization, the domain of interest $\mathcal{B}$ is discretized with n_{el} finite elements $\mathcal{B}_e$ as $\mathcal{B} = \bigcup_{e=1}^{n_{\text{el}}} \mathcal{B}^e$. We apply the isoparametric concept to interpolate the trial functions ϕ^h and the test functions $\delta\phi^h$ with the same shape functions N on the element level,

$$\delta\phi^h|_{\mathcal{B}^e} = \sum_{i=1}^{n_{\text{en}}} N^i\;\delta\phi_i\,, \quad \phi^h|_{\mathcal{B}^e} = \sum_{j=1}^{n_{\text{en}}} N^j\;\phi_j \tag{6}$$

where $i, j = 1, \ldots, n_{\text{en}}$ denotes the n_{en} element nodes. For the temporal discretization, the time interval of interest $\mathcal{T}$ is partitioned into n_{stp} subintervals $[t_n, t_{n+1}]$ as $\mathcal{T} = \bigcup_{n=0}^{n_{\text{stp}}-1} [t_n, t_{n+1}]$. The time increment of the current time slab is denoted as $\Delta t := t_{n+1} - t_n > 0$. To solve for the unknown action potential degrees of freedom ϕ at time t_{n+1}, we apply a standard backward Euler time integration scheme together with the following finite difference approximation of the first-order time derivative $\dot{\phi}$,

$$\dot{\phi} = \tfrac{1}{\Delta t}[\phi - \phi_n] \tag{7}$$

where the index $(\circ)_{n+1}$ has been omitted for the sake of clarity. With the spatial and temporal discretizations (6) and (7), the discrete algorithmic residual R^{ϕ}_I takes the following format:

$$\mathsf{R}^{\phi}_I = \mathop{\mathbf{A}}_{e=1}^{n_{\text{el}}} \int_{\mathcal{B}^e} N^i \frac{\phi - \phi_n}{\Delta t} + \nabla N^i \cdot \boldsymbol{q}\, \mathrm{d}V - \int_{\partial \mathcal{B}^e_q} N^i \bar{q}\, \mathrm{d}A - \int_{\mathcal{B}^e} N^i f^{\phi}\, \mathrm{d}V \doteq 0 \tag{8}$$

Herein, the operator $\mathbf{A}$ symbolizes the assembly of all element contributions at the element nodes $i = 1, \ldots, n_{\text{en}}$ to the overall residual at the global node points $I = 1, \ldots, n_{\text{nd}}$. We suggest solving the global residual problem (8) with the help of an incremental iterative Newton Raphson solution technique based on the consistent linearization of the residual R^{ϕ}_I which introduces the global iteration matrix K^{ϕ}_{IJ},

$$\mathsf{K}^{\phi}_{IJ} = \partial_{\phi_J} \mathsf{R}^{\phi}_I = \mathop{\mathbf{A}}_{e=1}^{n_{\text{el}}} \int_{\mathcal{B}^e} N^i \frac{1}{\Delta t} N^j + \nabla N^i \cdot \mathrm{d}_{\nabla\phi}\boldsymbol{q} \cdot \nabla N^j - N^i\, \mathrm{d}_{\phi} f^{\phi}\, N^j\, \mathrm{d}V \tag{9}$$

where $\mathrm{d}_{\nabla\phi}\boldsymbol{q} = \boldsymbol{D}$. The iterative update of the global vector of the unknowns ϕ_I at all n_{nd} nodes

$$\Delta\phi_I \leftarrow \Delta\phi_I - \sum_{J=1}^{n_{\text{nd}}} \mathsf{K}^{\phi\,-1}_{IJ}\, \mathsf{R}^{\phi}_J \quad \forall\, I = 1, \ldots, n_{\text{nd}} \tag{10}$$

follows straightforwardly from the inverse global iteration matrix $\mathsf{K}^{\phi\,-1}_{IJ}$ and the right-hand side vector R^{ϕ}_I. The recovery variable r needed to evaluate the source term $f^{\phi}(\phi, r)$ and its consistent algorithmic linearization $\mathrm{d}_{\phi} f^{\phi}(\phi, r)$ will be determined in the next subsection.

3.2 The recovery problem: local solution at the integration point level

The recovery variable r is introduced as an internal variable and stored locally on the integration point level. For the temporal discretization of recovery, we apply an implicit backward Euler time stepping scheme in combination with the following standard finite difference interpolation:

$$\dot{r} = \tfrac{1}{\Delta t}[\, r - r_n\,] \tag{11}$$

Analogous to the global non-linear action potential evolution, we suggest a local Newton iteration to evaluate the non-linear evolution equation for the recovery variable. To this end, Eq. (4) is cast into its residual format,

$$\mathsf{R}^r = r - r_n - \left[\left[\gamma + \frac{\mu_1\, r}{\mu_2 + \phi}\right][-r - c\,\phi\,[\phi - b - 1]]\right]\Delta t \doteq 0 \tag{12}$$

and linearized with respect to the unknown r,

$$\mathsf{K}^r = \partial_r \mathsf{R}^r = 1 + \left[\gamma + \frac{\mu_1}{\mu_2 + \phi}\,[\,2\,r + c\,\phi\,[\phi - b - 1]\,]\right]\Delta t \tag{13}$$

to render the incremental update of the recovery variable r at all integration points.

$$r \leftarrow r - \mathsf{K}^{r\,-1}\, \mathsf{R}^r \tag{14}$$

Having determined the current recovery variable, we can now evaluate the source term $f^{\phi} = c\,\phi\,[\phi - \alpha][1 - \phi] - r\,\phi$ for the right-hand side of the excitation problem (8). For the global Newton iteration (9), we finally need

to determine its consistent linearization based on the total derivative $\mathrm{d}_\phi f^\phi = \partial_\phi f^\phi + \partial_r f^\phi \, \mathrm{d}_\phi r$ which takes the following explicit representation.

$$\mathrm{d}_\phi f^\phi = c\,[\,-3\,\phi^2 + 2\,[1+\alpha]\,\phi - \alpha\,] - r - \phi\,\mathrm{d}_\phi r \tag{15}$$

The sensitivity of the recovery variable $\mathrm{d}_\phi r$ can be evaluated at local equilibrium $\mathrm{d}_\phi \mathsf{R}^r = \partial_\phi \mathsf{R}^r + \partial_r \mathsf{R}^r \, \mathrm{d}_\phi r \doteq 0$ as

$$\mathrm{d}_\phi r = -\mathsf{K}^{r\,-1}\,\partial_\phi \mathsf{R}^r \tag{16}$$

with

$$\partial_\phi \mathsf{R}^r = \left[\left[\gamma + \frac{\mu_1 r}{\mu_2 + \phi}\right] c\,[\,2\phi - b - 1\,] - \frac{\mu_1 r}{[\mu_2+\phi]^2}\,[\,r + c\,\phi\,[\,\phi - b - 1\,]\,]\right]\Delta t \tag{17}$$

where K^r is the local tangent operator given in Eq. (13). We will now illustrate the overall performance of the proposed computational algorithm in the context of re-entrant spiral waves in excitable cardiac tissue.

Remark 4 (Temporal discretization of the governing equations) In the present approach, we suggest to use an implicit finite difference based backward Euler scheme. Most approaches in the literature utilize explicit time integration schemes, e.g., [21,25]. Although some groups suggest fourth order Runge–Kutta methods, e.g., [32,33], we have found the backward Euler scheme extremely satisfying. We assume that the unexpectedly good performance of the backward Euler scheme can be traced back to the somewhat constrained nature of the action potential which, unlike most evolving variables in continuum mechanics, always returns to a unique stable equilibrium state.

4 Examples of re-entrant waves in cardiac tissue

This section is devoted to representative two- and three-dimensional numerical examples of cardiac excitation to illustrate the formation of re-entrant waves responsible for rhythmic disturbances in atrial and ventricular fibrillation. The formation of re-entry can have varied physiological origins. Most frequently, it is related to altered conduction properties in diseased cardiac tissue, e.g., caused by myocardial infarction. To computationally simulate the formation and stable rotation of physiologically realistic spiral waves it is essential to correctly capture the restitution properties of cardiac tissue. In stable resting tissue such as myocardium, two stimuli are needed to initiate a re-entrant wave pattern. The first stimulus is required to initiate a spatial gradient of recovery, whereas the second stimulus can consist of a simple single excitation in the repolarizing wave tail. The correct timing and location of the second stimulus, however, are extremely crucial. Their window of time and space is referred to as the vulnerable period. Provided the excited tissue sample is large enough, the retrograde propagation can initiate a self-sustained, re-entrant pattern of activation that continuously re-excites itself at a high but uncontrolled rate.

In what follows, we will demonstrate the ability of the finite-element based Aliev–Panfilov model to simulate the generation of spiral and scroll waves initiated by only small perturbations in the wave tail of an initially stable excitable system of cardiac muscle cells. In all initial boundary value problems, conversion of the non-dimensional action potential ϕ and time t to their physiological counterparts $\Phi\,[\mathrm{mV}]$ and $\tau\,[\mathrm{ms}]$ is carried out through $\Phi = [100\,\phi - 80]\,\mathrm{mV}$ and $\tau = [12.9\,t]\,\mathrm{ms}$. We consider square and cubic domains made up of ventricular cardiomyocytes with the material parameters $\alpha = 0.01,\ \gamma = 0.002,\ b = 0.15,\ c = 8,\ \mu_1 = 0.2$ and $\mu_2 = 0.3$. Unless stated otherwise, stable initial values of $\Phi_0 = -80\,\mathrm{mV}$ are assigned to the nodal action potential. Conduction is assumed to be isotropic $\boldsymbol{D} = d^{\mathrm{iso}}\boldsymbol{I}$ with $d^{\mathrm{iso}} = 0.2\,\mathrm{mm}^2/\mathrm{ms}$ for the two-dimensional examples in Sect. 4.1 and $d^{\mathrm{iso}} = 0.1\,\mathrm{mm}^2/\mathrm{ms}$ for the three-dimensional examples in Sect. 4.2.

4.1 Two-dimensional excitation: single and double spiral waves

For the two-dimensional generation of spiral waves, we consider a square $100\,\mathrm{mm} \times 100\,\mathrm{mm}$ domain of cardiac tissue discretized by 101×101 four-node quadrilateral elements (see Figs. 2, 3). Following the two stimulus initiation protocol described above, we initiate a horizontal planar wave at the left vertical edge through an external excitation realized by perturbing the initial nodal values of the action potential away from their stable

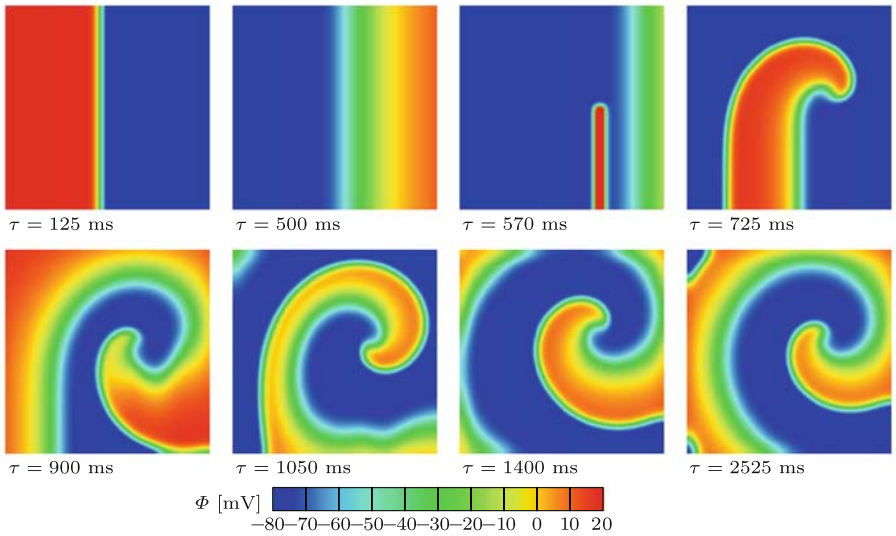

Fig. 2 Initiation, development, and rotation of single spiral wave re-entry in square block of cardiac muscle tissue. Initiation of planar wave through initial excitation of $\Phi_0 = -40\,\text{mV}$ at time $\tau = 0\,\text{ms}$ on *left* boundary. Initiation of spiral wave through external stimulation of $f^{\phi}_{\text{stim}} = 40$ at time $\tau = 570\,\text{ms}$ for $\Delta t = 10\,\text{ms}$ in *red domain* in the third snapshot

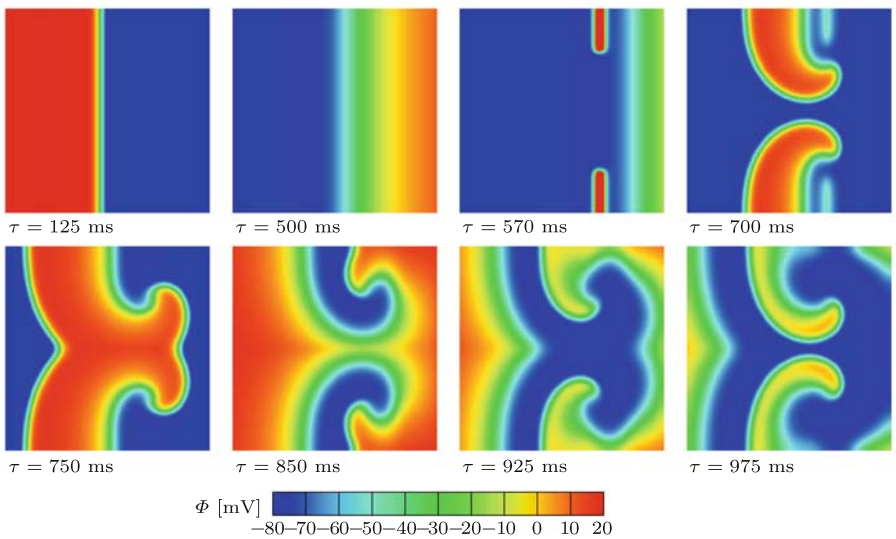

Fig. 3 Initiation, development, and rotation of double spiral wave re-entry in square block of cardiac muscle tissue. Initiation of planar wave through initial excitation of $\Phi_0 = -40\,\text{mV}$ at time $\tau = 0\,\text{ms}$ on *left* boundary. Initiation of spiral wave through external stimulation of $f^{\phi}_{\text{stim}} = 40$ at time $\tau = 570\,\text{ms}$ for $\Delta t = 10\,\text{ms}$ in *red domain* in the third snapshot

equilibrium state to $\Phi_0 = -40\,\text{mV}$. This perturbation has to be of sufficient amplitude and duration to excite the nodes closest to the stimulus, whereas cells further away from the stimulus are still at rest. At the border between the subthreshold and superthreshold, a steep wavefront is formed (see Fig. 2). This transition front then starts to travel in the horizontal direction, from left to right, depolarizing the entire domain (see the panel at $\tau = 125\,\text{ms}$ in Fig. 2). The shapshot taken at $\tau = 500\,\text{ms}$ illustrates how the repolarizing wave tail follows the wave front. To initiate a single spiral wave, we apply a second stimulus in the wave tail by slightly perturbing a small rectangular region bounded by the coordinates $x \in [67, 70]\,\text{mm}$ and $y \in [0, 50]\,\text{mm}$ with respect to the origin at the lower left corner. The selected region is depolarized by adding an external stimulus of $f^{\phi}_{\text{stim}} = 40\,\text{mV}$ to the source term f^{ϕ} in Eq. (3). External stimulation is performed at time $\tau = 570\,\text{ms}$ over the time period of $\Delta t = 10\,\text{ms}$. The panels belonging to the time steps following the perturbation clearly demonstrate that we have caught the vulnerable period properly: a single spiral wave develops in the tissue

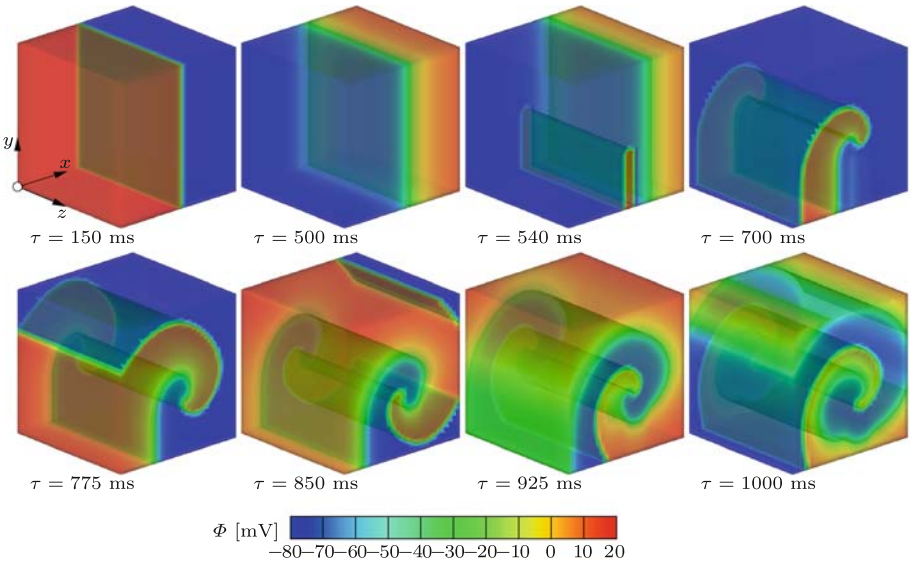

Fig. 4 Initiation, development, and rotation of a symmetric vortex wave re-entry in a cubic block of cardiac tissue. Initiation of planar wave through initial excitation of $\Phi_0 = 0\,\text{mV}$ at time $\tau = 0\,\text{ms}$ on the *left* boundary. Initiation of spiral wave through external stimulation of $f^{\phi}_{\text{stim}} = 10$ at time $\tau = 540\,\text{ms}$ for $\Delta t = 20\,\text{ms}$ in *red domain* in the third snapshot *upper row*

sample. Figure 2 clearly display the stages of initiation, development, and stable rotation of the excitation wave. Instead of returning to its stable rest state, the tissue sample undergoes an oscillatory excitation and is continuously re-excited through the clockwise rotating spiral waves.

Next, we elaborate the effect of a symmetric double perturbation by externally depolarizing the two rectangular regions in the wave tail which are bounded by the coordinates $x \in [67, 70]\,\text{mm}$, $y \in [0, 20]\,\text{mm}$ and $x \in [67, 70]\,\text{mm}$, $y \in [80, 100]\,\text{mm}$ with respect to the origin at the lower left corner. Again, we add an external stimulus of $f^{\phi}_{\text{stim}} = 40\,\text{mV}$ to the source term f^{ϕ} at time $\tau = 570\,\text{ms}$ for a duration of $\Delta t = 10\,\text{ms}$. The double perturbation initiates a set of symmetric spiral waves. The upper wave rotates in a clockwise fashion, whereas the lower wave rotates counterclockwise. The action potential distribution indicates the complex interaction of both wave fronts to form complex two-dimensional wave patterns. Their spatio-temporal evolution is illustrated in the time sequence shown in Fig. 3.

4.2 Three-dimensional excitation: symmetric and non-symmetric scroll waves

In the three-dimensional space, the planar spiral waves considered in the preceding examples appear in the form of complex scroll waves. We illustrate the formation of re-entrant scroll waves for two different perturbation scenarios that trigger different the re-entry patterns. To this end, we consider a cubic domain of cardiac muscle with edge lengths of 100 mm which is discretized into $31 \times 31 \times 7$ eight-node brick elements in the respective x,y and z directions (see Fig. 4). Similar to the previous two-dimensional examples, we apply a first stimulus to initiate a horizontally traveling planar wave by slightly increasing the initial values of the nodal action potential on the left vertical edge to $\Phi_0 = 0\,\text{mV}$ (see Fig. 4). Once the wave front has formed, it begins to travel horizontally, from left to right, depolarizing the three-dimensional domain (see the panel at $\tau = 150\,\text{ms}$ in Fig. 4). Similar to the two-dimensional example, the repolarizing wave tail follows the wave front as shown in the shapshot taken at $\tau = 500\,\text{ms}$. Once the wave tail has reached the right edge, we initiate a re-entrant scroll wave by externally perturbing a pre-defined part of the domain through a second stimulus. Again, we compare two different geometries of external stimulation that give rise to distinct shapes of re-entrant vortices. In the first case, a symmetric rectangular region bounded by the coordinates $x \in [50, 55]\,\text{mm}$, $y \in [0, 40]\,\text{mm}$ and $z \in [0, 100]\,\text{mm}$ is depolarized by adding an extra stimulus of $f^{\phi}_{\text{stim}} = 10\,\text{mV}$ to the source term f^{ϕ} at time $\tau = 540\,\text{ms}$ for $\Delta t = 20\,\text{ms}$ (see 4). The post-perturbation action potential distributions in the lower row of Fig. 4 demonstrate the stages of initiation, development, and stable rotation of the symmetric cylindrical scroll re-entries. The uniform cylindrical shape of the three-dimensional re-entrant wave is due to the uniform

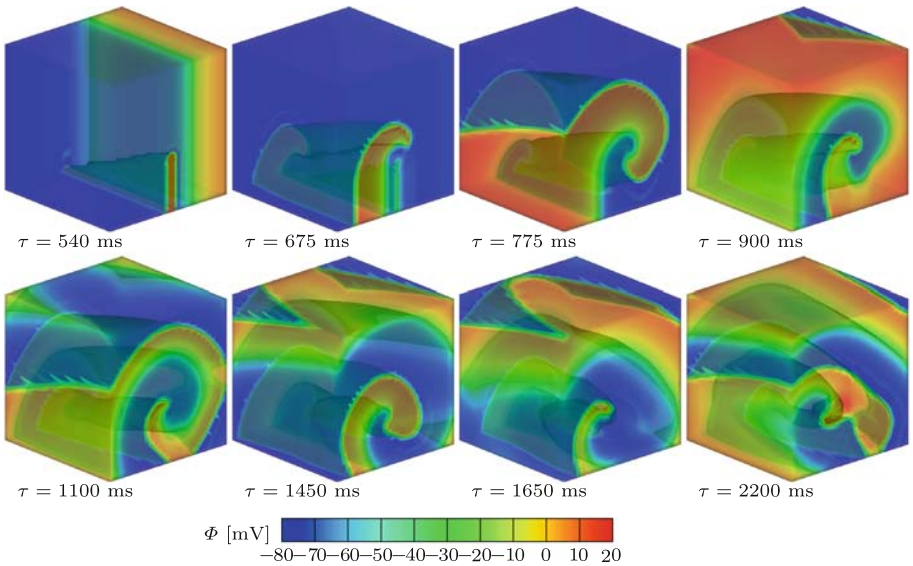

Fig. 5 Initiation, development, and rotation of a non-symmetric vortex wave re-entry in a cubic block of cardiac muscle tissue. Initiation of planar wave through initial excitation of $\Phi_0 = 0\,\text{mV}$ at time $\tau = 0\,\text{ms}$ on the *left* boundary. Initiation of spiral wave through external stimulation of $f^{\phi}_{\text{stim}} = 10$ at time $\tau = 540\,\text{ms}$ for $\Delta t = 20\,\text{ms}$ in *red domain* in the first snapshot

geometry of the uniform region of stimulation. In two-dimensional planar sections along the z axis, the wave pattern clearly resembles the single spiral wave pattern of the previous two-dimensional example.

To initiate a truly three-dimensional wave with an additional out-of-plane contribution, we consider a triangular depolarization region in lieu of the rectangular one. For this purpose, the height (y coordinate upper bound) of the region of stimulation is varied linearly from 0 to 40 mm along the z direction within the selected range of $x \in [50, 55]\,\text{mm}$. The snapshots in Fig. 5 depict the spatio-temporal generation and evolution of the three-dimensional scroll wave. In contrast to the former example, we observe that the ramp-shaped domain of perturbation gives rise to a complex vortex geometry. In this case, profiles of the waves in different xy planes are no longer in-phase but whir at different frequencies. The complex three-dimensional scroll wave is extremely difficult to follow even in this simple cubic domain. This last example clearly demonstrates how chaotic wave patterns can be generated through relatively regular perturbations. It is obvious that excitation patterns of this kind can have devastating consequences if they form in the ventricle and are not terminated quickly.

4.3 Three-dimensional excitation: generic bi-ventricular heart model

Last, we will illustrate the algorithm's feasibility to reproduce the formation of scroll waves in more complex geometries. Figure 6 illustrates a typical benchmark geometry for excitation modeling based on the generic representation of the left and right ventricle approximated by two nested ellipsoids [31]. The system is discretized with 13,348 four-node tetrahedral elements introducing a total of 3,059 nodes. The material parameters are similar to the previous three-dimensional example. After a smoothly propagating wave has been established by externally stimulating the atrioventricular node located at the central basal septum, we trigger the formation of a scroll wave by applying a slight perturbation in the repolarizing wave tail. Similar to the previous examples, we add an external stimulation of $f^{\phi}_{\text{stim}} = 20\,\text{mV}$ to the source term f^{ϕ} from time $\tau = 425\,\text{ms}$ to $\tau = 465\,\text{ms}$. This perturbation is applied to a small rectangular region of the anterior ventricular wall which turns into the initial center of the rotating wave. Figure 6 documents the initial formation of the scroll wave at τ =1,200 ms. The following snap shots at τ =1,800 ms, τ =2,400 ms, and τ =3,000 ms illustrate the evolution of the vortex wave re-entry. The upper row depicts the contour plots of the action potential Φ, the lower row depicts the vortical iso-surface images corresponding to $\Phi = 0\,\text{mV}$. The combination of the complex bi-ventricular geometry, the non-symmetric perturbation, and the homogeneous Neumann boundary conditions clearly triggers a chaotic non-stationary wave pattern with the center of the scroll moving from the septal basal to the apical lateral region. Unexpectedly, The lower row of translucent images also indicates the formation of a second scroll wave on the

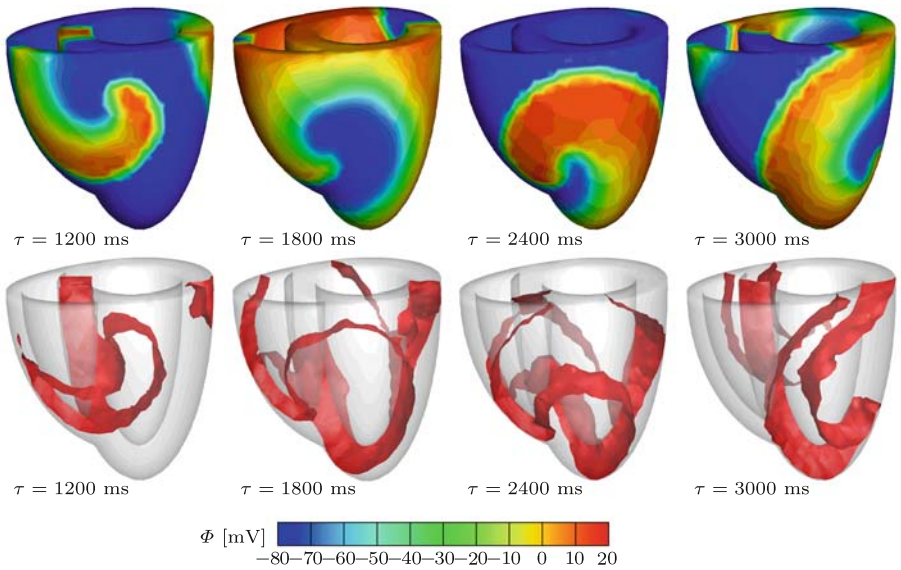

Fig. 6 Initiation, development, and rotation of a non-symmetric vortex wave re-entry in a generic bi-ventricular heart model at selected stages of the finite element simulation. The snapshots in the *upper row* depict contour plots of the action potential Φ, while the vortical iso-surface images corresponding to $\Phi = 0\,\mathrm{mV}$ in the *lower row* clearly demonstrate the two scrolls in the translucent model

posterior side. This example documents the feasibility of the proposed approach to reproduce the evolution of re-entrant scroll waves on cardiac geometries.

5 Discussion

In the healthy heart, the sinoatrial node acts as pacemaker and is responsible for the generation of a unique periodic signal of excitation. This signal travels through the atria, passes the atrioventricular node, and is transmitted through the ventricles via a complex cardiac conduction system of Purkinje fibers to ensure well-organized smooth contraction cardiomyocytes. In the normal heart, these muscle cells usually reside at a stable resting state. Unable to self-excite themselves, cardiomyocytes need to be stimulated by traveling excitation waves to perform a well-coordinated rhythmic contraction. In diseased hearts, locally altered conduction or excitation properties might trigger the formation of spiral wave patterns in which the originally stable cardiomyocytes keep re-exciting themselves to generate highly disorganized wave patterns. These patterns which are characteristic for atrial and ventricular fibrillation may prevent the heart from relaxing properly during its filling phase. To suppress re-entry of unsynchronized electrical signals, arrhythmia patients are typically prescribed antiarrhythmatic drugs. However, these drugs are only a means of reducing the probability of arrhythmatic episodes and serve to control the effects of the pathology. Currently, treatments such as surgical or radiofrequency ablation are being used to permanently treat fibrillation by removing tissue at sites where electrical re-entry or conduction is occurring. Implantable defibrillators are another possible treatment option.

To optimize medical treatment of atrial and ventricular fibrillation, it is essential to fully understand the generation of re-entrant spiral and scroll waves. In this manuscript, we have presented a novel computational algorithm to discretize the governing equations of cardiac electrophysiology in time and space. By discretizing the action potential globally on the node point level and the recovery variable locally on the integration point level, we have provided an efficient and highly modular discretization scheme. This approach might seem trivial to the computational mechanics community, but, to the best of our knowledge, it is novel to the computational cardiology community. Our particular cell model was based on the two-parameter Aliev–Panfilov model for cardiomyocytes, but other cell types can be implemented straightforwardly with only minor local modifications.

In contrast to most existing explicit time integration schemes, we suggest an unconditionally stable implicit backward Euler scheme for the temporal discretization of the action potential and the recovery variable. Robustness and quadratic convergence of the solution procedure are ensured through the incremental iterative Newton–Raphson scheme both globally for the action potential and locally for the recovery variable. We have

derived the consistent linearization of the excitation problem and the recovery problem. The advantage of applying a finite element solution in space combined with an implicit finite difference based scheme in time is its simplicity in the context of excitation–contraction coupling for monolithic finite-element based whole heart models. Coupling of excitation and contraction would manifest itself in additional source terms f^{ϕ}_{mech} in the action potential evolution mimicking the influence of mechanically activated ion channels. In turn, the evolution of the action potential would influence the mechanical contraction problem through active stresses of contraction along the direction of the cardiac muscle fibers.

The ability of the algorithm to correctly reproduce the formation of complex spiral and scroll type wave patterns has been demonstrated in two- and three-dimensional simulations of slightly perturbed smooth cardiac excitation. We have analyzed both regular square and cubic benchmark geometries and a more complex generic bi-ventricular heart model. We are currently exploring the potential of the algorithm in more realistic physiological patient-specific geometries generated from magnetic resonance images [17]. A current area of growing interest is the simulation of bi-ventricular pacing, a novel technique for cardiac resynchronization that stimulates the left and right ventricles simultaneously in the case of heart failure. Reliable, predictive finite element simulations seem to provide a promising tool to optimize locations, amplitudes, and frequencies of both pacemakers to generate optimal cardiac contraction.

Acknowledgments This material is based on work supported by the National Science Foundation under Grant No. EFRI-CBE 0735551 Engineering of cardiovascular cellular interfaces and tissue constructs and by the Hellman Faculty Scholar Fund. Dr. Serdar Göktepe was partly supported by the NIH Center for Biomedical Computation at Stanford Simbios. Jonathan Wong was supported through the Biomedical Computation Graduate Training Grant at Stanford 5T32GM063495-07.

References

1. American Heart Association.: Heart Disease and Stroke Statistics—2008 Update. American Heart Association, Dallas (2008)
2. Aliev, R.R., Panfilov, A.V.: A simple two-variable model of cardiac excitation. Chaos Solitons Fractals **7**, 293–301 (1996)
3. Beeler, G.W., Reuter, H.: Reconstruction of the action potential of ventricular myocardial fibers. J. Physiol. **268**, 177–210 (1977)
4. Berne, R.M., Levy, M.N.: Cardiovascular Physiology. Mosby, St. Louis (2001)
5. Bers, M.D.: Excitation-Contraction Coupling and Cardiac Contractile Force. Kluwer, Dordrecht (2001)
6. Clayton, R.H., Panfilov, A.V.: A guide to modelling cardiac electrical activity in anatomically detailed ventricles. Prog. Biophys. Mol. Biol. **96**, 19–43 (2008)
7. Fenton, F.H., Karma, A.: Vortex dynamics in three-dimensional continuous myocardium with fiber rotation: filament instability and fibrillation. Chaos **8**, 20–47 (1998)
8. Fenton, F.H., Cherry, E.M., Hastings, H.M., Evans, S.J.: Multiple mechanisms of spiral wave breakup in a model of cardiac electrical activity. Chaos **12**, 852–892 (2002)
9. FitzHugh, R.: Impulses and physiological states in theoretical models of nerve membranes. Biophys. J. **1**, 445–466 (1961)
10. Ganong, W.F.: Review of Medical Physiology. McGraw-Hill, NY (2003)
11. Göktepe, S., Kuhl, E.: Computational modeling of cardiac electrophysiology: a novel finite element approach. Int. J. Numer. Methods Eng. **79**, 156–178 (2009)
12. Göktepe, S., Kuhl, E.: Electromechanics of the heart—a unified approach to the strongly coupled excitation-contraction problem. Comput. Mech. (2009, in press)
13. Hodgkin, A.L., Huxley, A.F.: A quantitative description of membrane current and its application to conductance and excitation in nerve. J. Physiol. **117**, 500–544 (1952)
14. Hunter, P.J., McCulloch, A.D., ter Keurs, H.E.D.J.: Modelling the mechanical properties of cardiac muscle. Prog. Biophys. Mol. Biol. **69**, 289–331 (1998)
15. Keener, J., Sneyd, J.: Mathematical Physiology. Springer, Berlin (2004)
16. Klabunde, R.E.: Cardiovascular Physiology Concepts. Lippincott Williams & Wilkins, Philadelphia (2005)
17. Kotikanyadanam, M., Göktepe, S., Kuhl, E.: Computational modeling of electrocardiograms—a finite element approach towards cardiac excitation. Commun. Numer. Methods Eng. doi:10.1002/cnm.1273
18. Luo, C., Rudy, Y.: A model of the ventricular cardiac action potential. Depolarization, repolarization, and their changes. Circ. Res. **68**, 1501–1526 (1991)
19. Mines, G.R.: On the dynamic equilibrium of the heart. J. Physiol. **46**, 349–383 (1913)
20. Nagumo, J., Arimoto, S., Yoshizawa, S.: Active pulse transmission line simulating nerve axon. Proc. Inst. Radio Eng. **50**, 2061–2070 (1962)
21. Nash, M.P., Panfilov, A.V.: Electromechanical model of excitable tissue to study reentrant cardiac arrhytmias. Prog. Biophys. Mol. Biol. **85**, 501–522 (2004)
22. Noble, D.: A modification of the Hodgkin-Huxley equations applicable to Purkinje fibre action and pacemaker potentials. J. Physiol. **160**, 317–352 (1962)
23. Opie, L.H.: Heart Physiology: From Cell to Circulation. Lippincott Williams & Wilkins, Philadelphia (2003)
24. Panfilov, A.V., Nash, M.P.: Self-organized pacemakers in a coupled reaction-diffusion-mechanics system. Phys. Rev. Lett. **95**, 258104-1–258014-4 (2005)

25. Panfilov, A.V., Keldermann, R.H., Nash, M.P.: Drift and breakup of spiral waves in reaction-diffusion-mechanics systems. Proc. Natl. Acad. Sci. USA **104**, 7922–7926 (2007)
26. Plonsey, R., Barr, R.C.: Bioelectricity. A Quantitative Approach. Springer, Berlin (2007)
27. Rogers, J.M., McCulloch, A.D.: A collocation-Galerkin finite element model of cardiac action potential propagation. IEEE Trans. Biomed. Eng. **41**, 743–757 (1994)
28. Rogers, J.M., McCulloch, A.D.: Nonuniform muscle fiber orientation causes spiral wave drift in a finite element model of cardiac action potential propagation. J. Cardiovasc. Electrophysiol. **5**, 496–509 (1994)
29. Rogers, J.M.: Wave front fragmentation due to ventricular geometry in a model of the rabbit heart. Chaos **12**, 779–787 (2002)
30. Sachse, F.B.: Computational Cardiology. Springer, Berlin (2004)
31. Sermesant, M., Rhode, K., Sanchez-Ortiz, G.I., Camara, O., Andriantsimiavona, R., Hegde, S., Rueckert, D., Lambiase, P., Bucknall, C., Rosenthal, E., Delingette, H., Hill, D.L.G., Ayache, N., Razavi, R.: Simulation of cardiac pathologies using an electromechanical biventricular model and XMR interventional imaging. Med. Image Anal. **9**, 467–480 (2005)
32. Sermesant, M., Delingette, H., Ayache, N.: An electromechanical model of the heart for image analysis and simulation. IEEE Trans. Med. Imaging **25**, 612–625 (2006)
33. Sermesant, M., Peyrat, J.-M., Chinchapatnam, P., Billet, F., Mansi, T., Rhode, K., Delingette, H., Razavi, R., Ayache, N.: Towards patient-specific myocardial models of the heart. Heart Fail. Clin. **4**, 289–301 (2008)
34. ten Tuscher, K.H.W.J., Panfilov, A.V.: Modelling of the ventricular conduction system. Prog. Biophys. Mol. Biol. **96**, 152–170 (2008)
35. Zheng, Z., Croft, J., Giles, W., Mensah, G.: Sudden cardiac death in the United States. Circulation **104**, 2158–2163 (2001)